

Melting of Perennial Sea Ice in the Beaufort Sea Enhanced Its Impacts on Early-Winter Haze Pollution in North China after the Mid-1990s

YUYAN LI

Key Laboratory of Meteorological Disaster, Ministry of Education/Joint International Research Laboratory of Climate and Environment Change (ILCEC)/Collaborative Innovation Center on Forecast and Evaluation of Meteorological Disasters, Nanjing University of Information Science and Technology, Nanjing, China

ZHICONG YIN

Key Laboratory of Meteorological Disaster, Ministry of Education/Joint International Research Laboratory of Climate and Environment Change (ILCEC)/Collaborative Innovation Center on Forecast and Evaluation of Meteorological Disasters, Nanjing University of Information Science and Technology, Nanjing, Southern Marine Science and Engineering Guangdong Laboratory (Zhuhai), Zhuhai, and Nansen-Zhu International Research Centre, Institute of Atmospheric Physics, Chinese Academy of Sciences, Beijing, China

(Manuscript received 17 September 2019, in final form 17 March 2020)

ABSTRACT

In recent years, haze pollution has become the most concerning environmental issue in China due to its tremendous negative effects. In this study, we focus on the enhanced responses of December–January haze days in North China to September–October sea ice in the Beaufort Sea during 1998–2015. Via both observation and numerical approaches, compared with an earlier period (1980–97), the sea ice concentration in the Beaufort Sea presented large variability during 1998–2015. During 1980–97, the Beaufort Sea was mainly covered by perennial ice, and the ablation and freezing of sea ice mainly occurred at the south edge of the Beaufort Sea. Thus, heavy sea ice in autumn induced negative sea surface temperature anomalies across the Gulf of Alaska in November. However, the colder sea surface in the Gulf of Alaska only induced a weak influence on the haze-associated atmospheric circulations. In contrast, during 1998–2015, a drastic change in sea ice existed near the center of the Arctic Ocean, due to the massive melting of multiyear sea ice in the western Beaufort Sea. The perennial ice cover in the western Beaufort Sea was replaced by seasonal ice. The broader sea ice cover resulted in positive sea surface temperature anomalies in the following November. Then, suitable atmospheric backgrounds were induced for haze pollution in December and January. Simultaneously, the response of the number of haze days over North China to sea ice cover increased. These findings were verified by the CESM-LE simulations and aided in deepening the understanding of the cause of haze pollution.

1. Introduction

Since the beginning of the satellite-observed sea ice era, record-breaking minimum values of sea ice cover have been observed in 2007 and 2012 (Polyakov et al.

2017), which might be connected to the trends of sea level pressure (SLP) in Arctic in summer (Simmonds 2015). The dramatic reduction of the summer Arctic sea ice (ASI) extent in recent years has fundamentally changed the nature of the ice (Maslanik et al. 2011) including the trend of thinning (Kwok and Rothrock 2009; Cavalieri and Parkinson 2012), the prolonging of melting duration in summer (Markus et al. 2009), and the shift from perennial sea ice to young ice (Maslanik et al. 2011; Kwok 2018). By the mid-twenty-first-century, an absence of sea ice (Holland et al. 2006; Overland and Wang 2013; Alekseev et al. 2016) and decrease of sea ice duration (Wang et al. 2017) appear in model simulations. The absence of ice in the Beaufort Sea may be for

Denotes content that is immediately available upon publication as open access.

Supplemental information related to this paper is available at the Journals Online website: <https://doi.org/10.1175/JCLI-D-19-0694.s1>.

Corresponding author: Zhicong Yin, yinzhc@163.com

DOI: 10.1175/JCLI-D-19-0694.1

© 2020 American Meteorological Society. For information regarding reuse of this content and general copyright information, consult the AMS Copyright Policy (www.ametsoc.org/PUBSReuseLicenses).

up to two months (Wang and Overland 2015; Mudryk et al. 2018). The Beaufort Sea is one of the regions where sea ice has drastically shrunk in Arctic since 2007 (Wang and Overland 2015), and also the major region where multiyear sea ice has retreated (Mudryk et al. 2018). Maslanik et al. (2007) revealed that 57% of the sea ice in Beaufort Sea survived more than 5 years and 25% was over 9 years old in 1987. However, by 2007, the amount of sea ice older than 5 years had fallen to 7%. Since late 1990s, when sea ice passed through the southern part of Beaufort Sea, the survival of sea ice has been difficult and the continuous clockwise activity of multiyear ice was limited. On the one hand, the increased seawater heat flux from the Bering Strait has warmed the ocean (Shimada et al. 2006; Mizobata et al. 2010), inducing younger ice in the areas where sea ice melts in summer (Rigor et al. 2002; Maslanik et al. 2007) and delaying the regrowth of sea ice in the autumn (Steele et al. 2008). On the other hand, multiyear sea ice was removed by transporting and melting activities in the western Arctic basin, a new region for ice export. Furthermore, the enhanced circulation did not help to replenish the old ice, but rather facilitated the transition to a younger ice cover. If multiyear ice continues to decrease, the Arctic ice cover will be controlled by the young ice, which is more sensitive to climate forcing (Kwok 2018).

The decrease in sea ice was possibly affected by the temporal and spatial changes in atmospheric circulation (Overland and Wang 2010; Screen et al. 2018), especially the changes of Arctic storms (Simmonds et al. 2008; Simmonds and Keay 2009; Screen et al. 2011). The changes of cyclone properties (such as frequencies, track, distribution, and depth), especially the interannual variations, are associated with the anomalous SLP, surface wind, sea ice drift, and cloud cover, which favor sea ice melting (Simmonds et al. 2008; Simmonds and Keay 2009; Screen et al. 2011). The loss of ASI can be traced back to Arctic warming, which reduces the speed of the eastward Rossby wave in the upper atmosphere and causes the relevant anomalous atmospheric circulation (Francis and Vavrus 2012; Vihma 2014; Zhou 2017). Lee et al. (2017) emphasized the importance of the downward net surface infrared radiation in the trend of Arctic surface warming, which was associated with the trend of moisture flux. The increase of moisture not only occurs from inside the Arctic basin (Lee et al. 2017) but also is imported from the midlatitudes (Luo et al. 2017). Luo et al. (2017) found that the Ural blocking during positive North Atlantic Oscillation would cause sea ice reduction over the Barents and Kara Seas, with more moisture intrusion into the Arctic. In addition, the Barents and Kara Seas warming associated with sea ice reduction was found to affect the mean duration of Ural

blocking events (Luo et al. 2018). Blackport and Screen (2020) used numerical simulations to find that Arctic amplification will cause significant reduction in the intensity of westerly wind, and pointed out it is reasonable to associate the Arctic amplification with slower westerly flow, at least qualitatively, but not with wavier circulation.

Screen and Simmonds (2010a,b) hold the view that the loss of sea ice cover in autumn and winter would enhance the transfer of heat and cause warmer air temperatures. Furthermore, the reduced ASI in autumn warms the Arctic and influences structured planetary waves in winter, which reduces the stability of the atmosphere and enhances baroclinicity (Gao et al. 2015). Many scholars have paid attention to the effect of ASI on Eurasian climate change, including effects on the East Asian jet stream and deep trough over East Asia (Li and Wang 2013) and the winter monsoon (Li and Wang 2014; Li et al. 2015; Wang and Liu 2016). The variations in ASI have had evident impacts on extreme temperature (Tang et al. 2013; Luo et al. 2019), extreme precipitation (Wu and Zhang 2009; Guo et al. 2014), snowstorms (Na et al. 2012), and dust events (Fan et al. 2017) in China. The frequency of dust and sandstorm events in North China is closely linked to the variability in ASI after the mid-1990s (Fan et al. 2017). The reduction in winter ASI is favorable for decreased snow cover in winter and spring, which excites eastward and southward stationary Rossby waves. Induced dust-associated atmospheric circulations, including the intensified East Asian subtropical jet, strengthened cyclogenesis, and increased atmospheric thermal instability, cause lower frequencies of dust events. Long-lived Ural blocking in conjunction with a positive phase of the North Atlantic Oscillation is conducive to amplifying the winter warm Arctic–cold Eurasian pattern (Luo et al. 2016). Bader et al. (2011) indicated that the ASI has a close link with the North Atlantic Oscillation. However, Hopsch et al. (2012) compared the relationship between the North Atlantic Oscillation and ASI during 1979–2010 and 1950–2010, and found that the results were inadequately robust. There are also some studies showing that the correlation between ASI in autumn and the East Asian winter monsoon is unstable after the 1990s (Li and Wang 2014; Gao et al. 2015).

High and quasi-linear anthropogenic emissions are well-known and fundamental drivers of the severe air pollution in China, but fluctuations in haze pollution on synoptic and interannual time scales seemingly show contradictory with increasing population and industrialization. Based on statistical energy consumption (Yin et al. 2015) and numerical experiments

(Dang and Liao 2019), anthropogenic emissions have been proven to mainly affect the long-term trend of haze pollutions. When the numerical simulations were solely driven by varying emissions (i.e., the meteorological conditions were fixed), the interannual to decadal variations of haze cannot be reproduced (Dang and Liao 2019). On the other hand, many researchers have discovered the importance of atmospheric circulation and local meteorological conditions in driving haze pollution across China (Wang and Chen 2016; Yang et al. 2016; Yin and Wang 2017a). By restricting the vertical and horizontal dispersion capacities, some meteorological conditions such as southerly anomalies, lower boundary layer height (BLH), higher relative humidity, and weak surface wind speed (WSPD) could induce and aggravate haze pollution (Yang et al. 2016; Yin and Wang 2017a). Wang et al. (2015) also illustrated the strong negative correlation between haze in eastern China and ASI during 1979–2012, which provided the theoretical basis for the seasonal outlook of haze days in North China (Yin and Wang 2016a, 2017b). Furthermore, Yin et al. (2019) revealed the physical mechanisms behind the close relationship between early autumn Beaufort Sea ice and December–January haze days in North China. Sea ice anomalies can induce anomalous SST over the Bering Sea and Gulf of Alaska. As a teleconnection, SST anomalies will cause northward westerly jet movement, weakening the East Asian deep trough in the following December and January. Thus, horizontal and vertical dispersion are restricted, which is conducive to haze formation. Therefore, the open question raised here is whether the connection between the ASI and early winter haze pollution in North China discussed by Yin et al. (2019) is stable or has changed on the interdecadal scale, and furthermore whether the melting multiyear sea ice affects this process and even causes the changes of relationship. Li et al. (2019) used the ensemble scheme of the WRF-Chem model to improve the prediction skill of $PM_{2.5}$ concentrations. The instabilities of the preceding drivers alter the predictability of haze days on seasonal to interannual scales. The goal of this study is to examine the changed response of early-winter haze days in North China to sea ice after the mid-1990s.

2. Datasets and methods

The definition of haze days was based on the results of Yin and Wang (2016b). To analyze the climatic features and variability of haze in China, haze days were calculated based on long-term meteorological observations. A day when the visibility was less than 10 km, with relative humidity lower than 90%, was described as a haze

day. Other weather phenomena that affected visibility, such as dust, sandstorms, and precipitation, were excluded. Furthermore, to demonstrate the representation of haze pollution, Yin and Wang (2016b) compared this data to atmospheric compositions (including SO_2 , NO , NO_2 , NO_x , CO , O_3 , $PM_{2.5}$, and nephelometric turbidity). Their results showed that these atmospheric compositions were consistent with the defined haze days. The relevant data, including the relative humidity, visibility, wind, and weather phenomena from 1980 to 2015, were downloaded from the National Meteorological Information Center, China Meteorological Administration.

The data on the age of sea ice (spatial resolution: $12.5\text{ km} \times 12.5\text{ km}$) were downloaded from the National Snow and Ice Data Center. Based on the sea ice concentration, perennial sea ice was recognized when the age of ice was longer than 1 year (Tschudi et al. 2019). Sea ice is considered to exist in each grid when the concentration of ice exceeds 15%. If the ice concentration is maintained at 15% or more throughout the summer (ice melting season), the age of the sea ice increases by one. The $1^\circ \times 1^\circ$ monthly sea ice concentrations were obtained from the Met Office Hadley Centre (Rayner et al. 2003). The geopotential height, SLP, zonal and meridional winds, surface wind and wind speed, vertical velocity, specific humidity, air temperature at different levels, surface air temperature, sea surface temperature (SST), skin temperature (SKT), and BLH were collected from the ERA-Interim datasets, with a horizontal resolution of $1^\circ \times 1^\circ$ (Dee et al. 2011). The daily reanalysis data from ERA-Interim datasets ($1^\circ \times 1^\circ$) included latent heat net flux and sensible heat net flux (Dee et al. 2011).

The numerical experiment dataset ($0.9^\circ \times 1.25^\circ$) was simulated with the fully coupled Community Earth System Model (CESM), which is maintained by the National Center for Atmospheric Research (Kay et al. 2015). The CESM was developed on the basis of the Common Climate System Model in 2010. It is a fully coupled global climate model that includes modules for atmosphere, land, ocean, ice, and rivers. All 35 members of the CESM Large Ensemble Project (<http://www.cesm.ucar.edu/projects/community-projects/LENS/>), which were subject to the same radiative forcing and started from a set of initial atmospheric states, are used in this study. The focus period (1980–2015) consists of a historical simulation (1980–2005) and representative concentration pathway (RCP) 8.5 forcing simulation (2006–15).

The anthropogenic emissions mainly affect the long-term trend of haze pollution (Yin et al. 2015; Dang and Liao 2019). The signal of global warming existed in

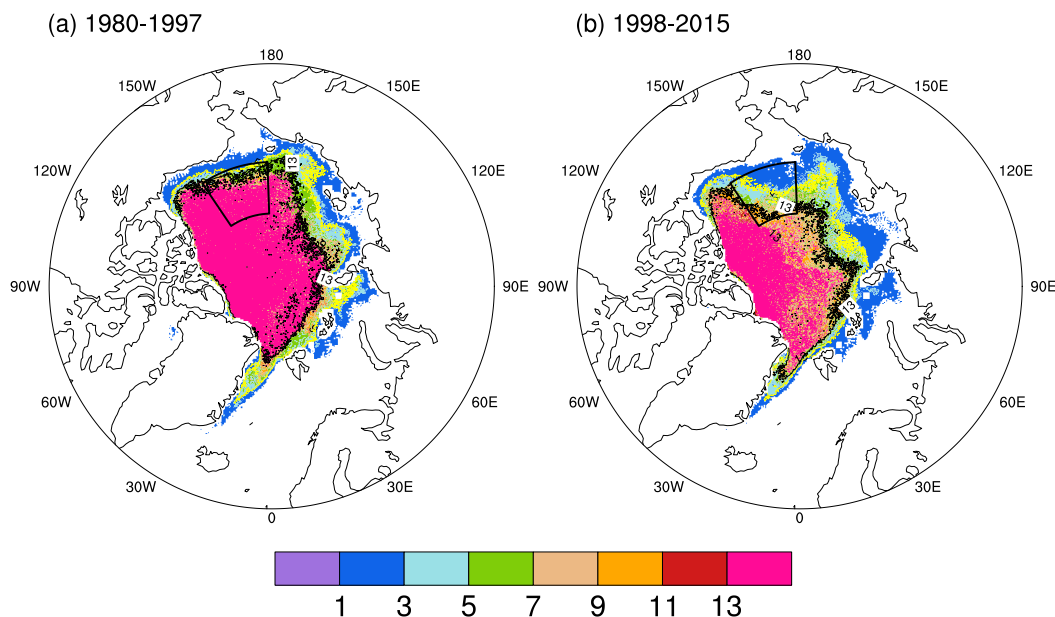


FIG. 1. The distribution of maximum durative years of multiyear sea ice (shading) during (a) 1980–97 and (b) 1998–2015. The black lines indicate that the number of years of multiyear ice exceeded 13 years. The yellow lines indicate that the number of multiyear ice exceeded 7 years. The black box represents the selected Beaufort Sea region.

most climate variables. Because we focused on the interannual-to-decadal variation of haze pollution, the linear trends of all variables were removed to exclude the effects of global warming and anthropogenic emissions.

3. Varying features of sea ice

To investigate the changes in sea ice itself, we first examined the age of sea ice in the Arctic (see Fig. S1 in the online supplemental material). Perennial ice was maintained in the north of the Beaufort Sea before 1998 and declined rapidly afterward. Before the mid-1990s, the average age of sea ice was more than 3 years over the Beaufort Sea (where was almost covered with perennial sea ice). Multiyear sea ice has persisted for more than 13 years in the north-central Beaufort Sea (Fig. 1a). In contrast, during 1998–2015, the phenomenon of multiyear ice melting appeared in the northern part of the Beaufort Sea (Fig. 1b), which had previously been covered by perennial sea ice (Fig. 1a). In this area, the maximum duration of multiyear ice has also plummeted (from more than 13 years to less than 7 years). A maximum duration of multiyear ice exceeding 9 years solely exists in the northernmost areas of the Beaufort Sea. The longest duration of multiyear ice in most parts of the north of Beaufort Sea is 3–7 years, and no multiyear ice exists in the southern region.

The continued losses of multiyear ice, which meant that Arctic ice cover was controlled by seasonal ice, should be considered as a more sensitive contributor to climate forcing (Kwok 2018). The changing state of the sea ice cover is also closely related to the existence of multiyear ice. Decreased multiyear sea ice in the Beaufort Sea would obviously reduce the coverage (Polyakov et al. 2012; Kwok 2018). As shown in Fig. 2a, the September–October sea ice area in Beaufort Sea (73° – 80° N, 146° – 178° W), defined as the BSISO index, varied slightly before the mid-1990s because perennial sea ice persistently covered the sea surface (Fig. 1a). However, after 1998, the sea ice area strongly varied (Fig. 2a) due to the replacement of perennial ice with annual ice (Fig. 1b). The relative standard deviation (RSD; i.e., the standard deviation/mean) of BSISO was also calculated, which increased from 8% during 1980–97 to 39% in the period of 1998–2015 and meant stronger modulation effects on the atmosphere circulation after 1998. The sea ice area in the north of Beaufort Sea (BSI_N) and in the south of Beaufort Sea (BSI_S), divided at 76° N, together constitute the BSISO and are shown in Fig. 2a. The RSD of BSI_S (BSI_N) was 16% (1%) during 1980–97 and 73% (29%) from 1998 to 2015. It is obvious that the BSI_N values were really flat before the mid-1990s, began to vary after 1998, and have strongly changed since 2006 (Fig. 2a). Because of the invariability of perennial ice area before the mid-1990s, the BSISO

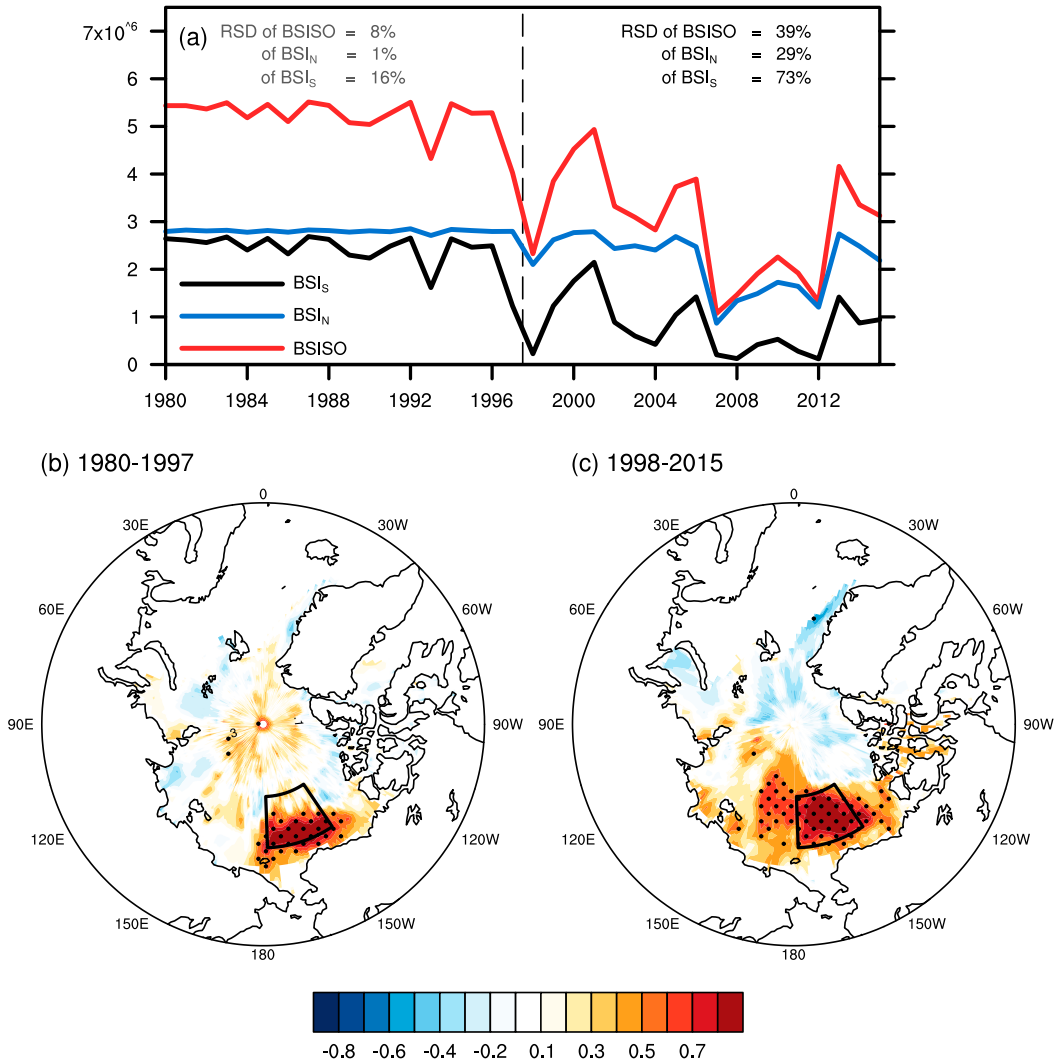


FIG. 2. (a) Variation in BSISO, BSI_N, and BSI_S and their RSD during P1 and P2. The correlation coefficient (CC) between the BSISO and September–October sea ice concentration during (b) 1980–97 and (c) 1998–2015 after detrending. The black dots indicate CCs exceeding the 95% confidence level (*t* test). The black box represents the selected Beaufort Sea region. The linear trend was removed.

changed only a little. However, after 1998, due to the replacement of perennial ice with annual ice, especially in the north of the Beaufort Sea, the BSISO showed obvious interannual variation.

The BSISO index, including both of the changing features of multiyear ice and young ice, emphasizes the coverage of sea ice and the impacts on high albedo and heat exchange. To clearly show the change of sea ice, the correlation coefficients between sea ice and the BSISO and the standard deviations of sea ice during 1980–97 (P1) and 1998–2015 (P2) are shown in Figs. 2b and 2c, respectively (see also Fig. S2). The September–October sea ice correlation with the BSISO was broader and the

correlation coefficients were also greater during P2 (Fig. 2b), indicating that the sea ice covaried more within the whole Beaufort Sea and could influence the local and teleconnected climate more significantly. However, during P1 the correlation coefficient was insignificant over the northern Beaufort Sea, but was significant close to the Bering Strait (Fig. 2b) (i.e., slightly southward of the selected key area). Furthermore, we calculated the spatial distribution of the standard deviation of the sea ice concentration during these two periods (Fig. S2). It is notable that the area with a larger standard deviation was mainly located in the peripheral band of the Arctic Ocean during P1 (Fig. S2a). However,

during P2, the larger standard deviation area, which indicates strong air–ice interactions, was mostly located inside the Arctic Circle (even close to the pole). That is, the evident intensity of the interannual variation in sea ice could be seen across the whole Beaufort Sea during P2, but was only visible in the marginal area of the Beaufort Sea during 1980–97, which is in good accordance with and possibly resulting from the replacement of perennial ice with annual ice.

Due to the high albedo of sea ice, the efficient radiative cooling could reflect more solar radiation and prevent the exchange of sea and air energy (Peng et al. 2019). Thus, significant variation in sea ice coverage would cause related SKT anomalies. Significant differences in the impacts of heavy sea ice on the surface temperature are easily and clearly recognizable from P1 and P2 (Fig. S3), which is consistent with the changing features of sea ice itself (ice age in Fig. 1, covariation in Fig. 2, and standard deviation distributions in Fig. S2). During P1, the significant variability of BSISO almost entirely came from sea ice from the south of Beaufort Sea. Analogously, significant negative correlations between September–October SKT and BSISO were narrowly located in the southern Beaufort Sea (Fig. S3a). It is worth noting that SKT in the Gulf of Alaska also shows significant decreases, indicating a synchronous change with the negative September–October SKT anomalies in the Beaufort Sea. In contrast, melting of perennial sea ice introduced large variability (indicating large air–ice interactions) into the north of the Beaufort Sea during P2. The area of significant negative SKT anomalies was not only extended but also located northward (Fig. S3b). As indicated by the negative relationship between the BSISO and SKT, the radiative cooling effect associated with the sea ice anomalies in the Beaufort Sea also exhibited significant differences during P1 and P2, which must have led to distinct responses in the resultant winter atmosphere circulations.

4. Strengthened impacts of BSISO on haze

The number of December and January haze days in North China (NC; 34°–42°N, 114°–120°E), denoted as HDJ_{NC}, showed obvious interannual variation during 1980–2015 after detrending (Fig. 3). Before the mid-1990s, the amplitudes of the number of haze days were small. After that, the intensity of the interannual-to-decadal variation in HDJ_{NC} strengthened. In addition, the number of haze days increased sharply after 2010. To reveal the connection between the HDJ_{NC} and ASI, their correlation coefficients were calculated and showed a significantly positive correlation in the

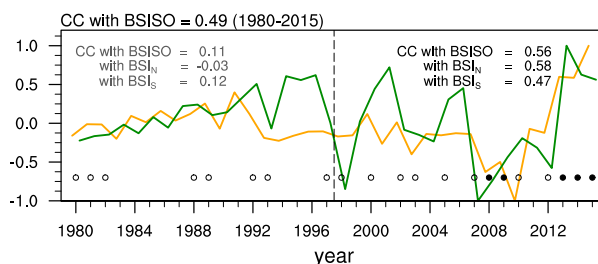


FIG. 3. The variation in normalized HDJ_{NC} (orange) and BSISO (green) from 1980 to 2015 after the removal of the linear trend. The open circle (O) indicates the anomalies of HDJ_{NC} and BSISO with the same mathematical sign. The closed circle (●) indicates the anomalies of HDJ_{NC} and BSISO both with the same mathematical sign and significant amplitudes (i.e., |anomalies| > 0.8 × its standard deviation). The CCs between HDJ_{NC} and BSISO, BSI_N, and BSI_S were also marked during 1980–97 and 1998–2015, respectively.

Beaufort Sea during 1980–2015 (figure omitted). Statistically, more sea ice coverage over the Beaufort Sea was associated with heavy haze pollution in North China. Furthermore, we found that this relationship became stronger after the mid-1990s. To explore the changes in the relationship between the BSISO index and HDJ_{NC}, the variations in HDJ_{NC} and BSISO and their corresponding relationships are plotted in Fig. 3. Obviously, the interannual-to-decadal fluctuations in both indices during P1 were weaker than those from 1998 to 2015. Simultaneously, the sharp increase in the number of haze events since 2010 was consistent with the phenomenon of growing sea ice cover after removing the linear trend. The number of years when the anomalies of HDJ_{NC} and BSISO with the same mathematical sign (NY_{SMS}) were counted and those with significant amplitudes (i.e., |anomalies| > 0.8 × its standard deviation) among the NY_{SMS} values was extracted and termed NY_{SA}. Compared to P1, both NY_{SMS} and NY_{SA} significantly increased during P2. Specifically, there were 8 (0) NY_{SMS} (NY_{SA}) years before the mid-1990s, which dramatically increased to 13 (5) years during 1998–2015 (Fig. 3).

The correlation coefficient between HDJ_{NC} and BSISO was 0.49 (exceeding the 99% confidence level) during 1980–2015; however, it changed to 0.11 (insignificant) and 0.56 during P1 and P2, respectively (Fig. 3). The changed relationship between the HDJ_{NC} and BSISO indicates that the response of HDJ_{NC} to Beaufort Sea ice significantly enhanced after the mid-1990s. Combining the previous analysis of sea ice coverage in two subperiods, we speculated that the varying features of sea ice, such as the covariation and intensity of the interannual variation, might have caused the observed strengthened relationship between HDJ_{NC}

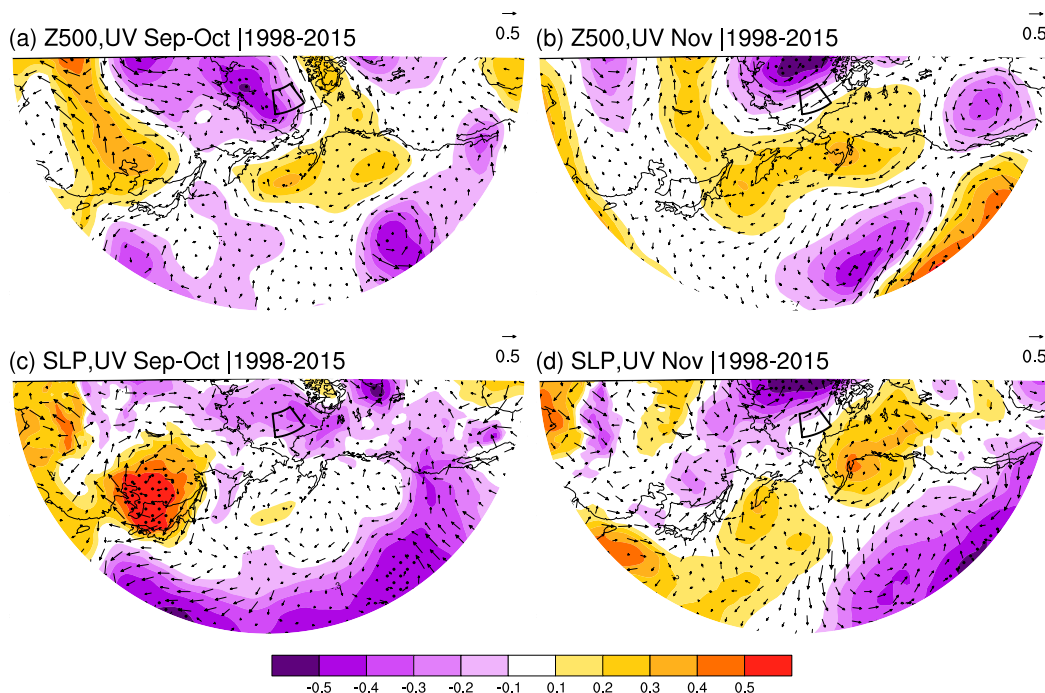


FIG. 4. The CCs between the BSISO and (a) September–October geopotential height (shading) and wind (arrow) at 500 hPa, (b) November geopotential height (shading) and wind (arrow) at 500 hPa, (c) September–October SLP (shading) and surface wind (arrow), and (d) November SLP (shading) and surface wind (arrow) during 1998–2015 after detrending. The black dots indicate CCs exceeding the 95% confidence level (t test). The black box in (a)–(d) represents the location of the Beaufort Sea.

and BSISO. As aforementioned, due to the replacement of perennial ice with annual ice in the north of Beaufort Sea, the variability of BSI_N largely contributed to the interannual to decadal variation in BSISO after 1998 (Fig. 2a). Correspondingly, the enhancement of correlation with HDJ_{NC} was more remarkable in the north of Beaufort Sea than in the south. That is, the correlation coefficient between HDJ_{NC} and BSI_N increased from -0.03 (insignificant in P1) to 0.58 (significant at 99% confidence level in P2). In contrast, the correlation coefficient between HDJ_{NC} and BSI_S increased from 0.12 (insignificant in P1) to 0.47 (significant at 95% confidence level in P2). This also illustrates that the melting of perennial sea ice (particularly in the north of Beaufort Sea) not only increased the variability of BSISO, but also enhanced the impacts of BSISO on the early-winter haze pollutions in North China after the mid-1990s.

5. Possible physical mechanisms

To further explore the reasons for this enhanced relationship, first, the associated atmospheric circulations were analyzed during P2 (Fig. 4) and P1 (Fig. 5). According to the results from Deser et al. (2007), the

responses of atmospheric circulations to sea ice anomalies were barotropic and strengthened within 2 months. In September and October, the anomalous radiation cooling effects induced anomalous cyclonic circulations from the surface to the mid- to high troposphere near the Beaufort Sea (Figs. 4a and 5a). During P2, anomalous cyclonic responses were located in the Arctic Ocean, which was consistent with the notable anomalous SKT region during P2 (Fig. S3b). In contrast, the center of the anomalous cyclonic circulations during P1 lay over the Gulf of Alaska and extended to the Beaufort Sea, which was close to the negative SKT anomalies during P1 (Fig. S3a and Fig. 5a). Moreover, there were shallow anticyclonic responses south of the cyclonic anomalies, in the North Pacific during P2 (Fig. 4a) or the Pacific center during P1 (Fig. 5a). In the subsequent November, the barotropic structure became more distinct (Figs. 4b,d and 5b,d). In particular, near the surface, weaker cyclonic and anticyclonic responses in September (Fig. 5a) and October became obvious in November. During P2, cyclonic and anticyclonic anomalies were still located in the Arctic Ocean in November, but the centers of these responses shifted eastward and northward, respectively (Figs. 4b,d). However, due to the obviously faster eastward movement during P1, the

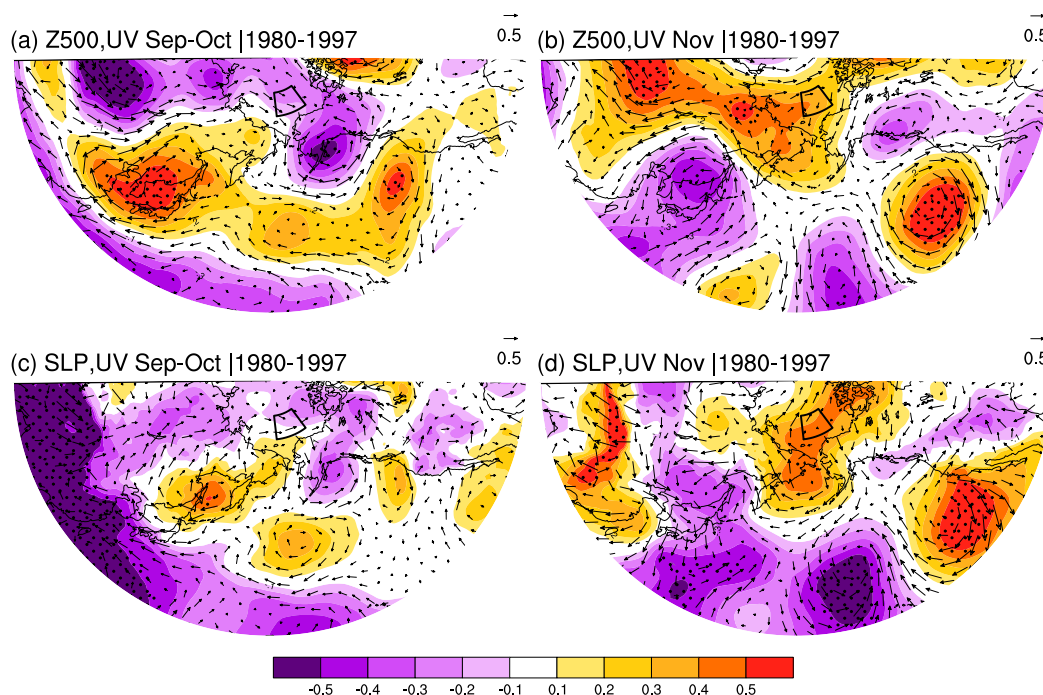


FIG. 5. The CCs between the BSISO and (a) September–October geopotential height (shading) and wind (arrow) at 500 hPa, (b) November geopotential height (shading) and wind (arrow) at 500 hPa, (c) September–October SLP (shading) and surface wind (arrow), and (d) November SLP (shading) and surface wind (arrow) during 1980–97 after detrending. The black dots indicate CCs exceeding the 95% confidence level (t test). The black box in (a)–(d) represents the location of the Beaufort Sea.

center of the low pressure system had moved toward land near the Mackenzie River, and the anomalous cyclone circulations over the Beaufort Sea were replaced by propagated anticyclonic anomalies (Figs. 5b,d). Thus, the associated atmospheric circulations influenced by the changed sea ice (i.e., the multiyear ice, the sea ice edge, and radiation cooling effect) presented significant differences mentioned in the above during P1 (Fig. 1a) and P2 (Fig. 1b), and these discrepant atmospheric anomalies near the Beaufort Sea and Gulf of Alaska in November might have triggered different responses on the sea surface, such as SST anomalies.

As illustrated in Fig. 6, obvious SST anomalies in November connected with the variation in the BSISO existed in the Gulf of Alaska area (GA; 46°–65°N, 130°–170°W; Fig. 6a) during P1 but in the Bering Sea and Gulf of Alaska (BA; 49°–60°N, 165°W–180° and 40°–52°N, 130°–165°W, respectively; Fig. 6b) during P2. In these two periods, the SST anomalies were not only in outlier regions but even manifested as opposite responses (i.e., negative anomalies during P1 and positive anomalies during P2). The aforementioned analysis indicated that the change in multiyear ice would invoke considerably different anomalous responses in the troposphere. The opposite SST variations during P1 (negative anomalies)

and P2 (positive anomalies) might be related to the atmospheric anomalies. The possible physical processes might be that the positive BSISO could affect the November WSPD in the North Pacific, as it might influence the energy budget of seawater and cause anomalous SST responses (Subrahmanyam et al. 2009). In addition, the positional differences in the anomalous cyclonic and anticyclonic circulations during P1 and P2, induced by the significant variation in sea ice coverage, would affect SSTs in different regions respectively (GA and BA; Figs. 6a,b). These discrepancies in the associated November SST anomalies during P1 and P2 might evoke distinctive responses in the atmosphere in the following December and January and cause the enhanced responses of December–January haze days in North China. Before exploring how SST anomalies affect haze days, the physical process of inducing these SST anomalies should be analyzed in more detail.

According to the correlation coefficients between the BSISO and WSPD, a highly correlated area was located near the southern part of the Bering Sea (RS1; 44°–54°N, 152°–180°W) and west of Canada (RS2; 44°–56°N, 130°–145°W) during P1 (Fig. 7a) but was distributed near the southern part of the Gulf of Alaska (RS3; 41°–54°N, 130°–165°W) during P2 (Fig. 7b). These November

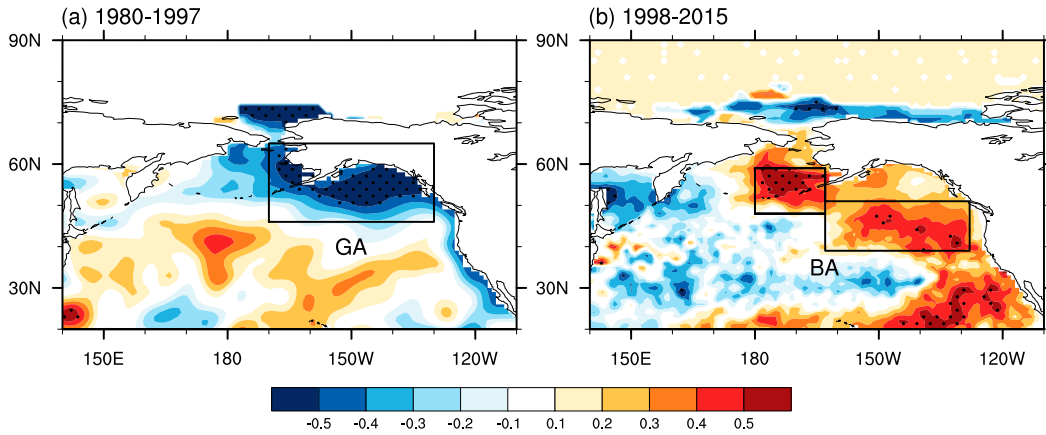


FIG. 6. The CCs between the BSISO and SSTs in November during (a) 1980–97 and (b) 1998–2015 after detrending. The black dots indicate CCs exceeding the 95% confidence level (t test). The black boxes (GA: Gulf of Alaska; BA: Bering Sea and Gulf of Alaska together) represent the significantly correlated areas, which were used to calculate the SST indices. The linear trend was removed.

WSPD anomalies were connected with the airflow over the southern part of the cyclonic and anticyclonic anomaly regions. During P2, the anomalous eastward flow, which was located over the southern part of the anomalous anticyclonic circulation region (Fig. 4d), overlaid the climatic westerlies and decelerated the WSPD in RS3. The area-averaged surface wind speed was computed as the WSPD index to explore the impacts on simultaneous latent heat and sensible heat fluxes, which were closely bound with the SST. The low $WSPD_{RS3}$ (i.e., the reduction of wind speed in RS3) weakened the local exchange of energy and water evaporation and decreased the release of latent heat and sensible heat (Fig. 8b). The pivotal areas of anomalous latent heat and sensible heat responses were located in the Gulf of Alaska and Bering Sea. Thus, the thermal energy was stored over BA, causing abnormally positive SSTs in November. Moreover, the anticyclonic

anomalies, under clear-sky conditions, caused the attenuation of solar radiation to weaken. Thus, more shortwave radiation was absorbed and stored in seawater, and positive SST anomalies appeared (Wu and Kinter 2011). Analogously, during P1, the anomalous eastward flow over the southern part of the anticyclonic anomaly region (Fig. 6d) decelerated the WSPD (RS1). Instead, the anomalous westward wind over the southern part of the cyclonic anomaly region could accelerate the WSPD (RS2). Thus, the WSPD index during P1 was constructed as the area-average WSPD in RS2 minus that in RS1 and is presented as $WSPD_{RS2-RS1}$. The combined effect of the WSPD in RS1 and RS2 enhanced the release of latent and sensible heat (Fig. 8a) in GA, causing abnormally negative SSTs.

In succession, the SST indices, that is, SST_{GA} (Gulf of Alaska area) and SST_{BA} (Bering Sea and Gulf of Alaska), were computed to probe the effects on

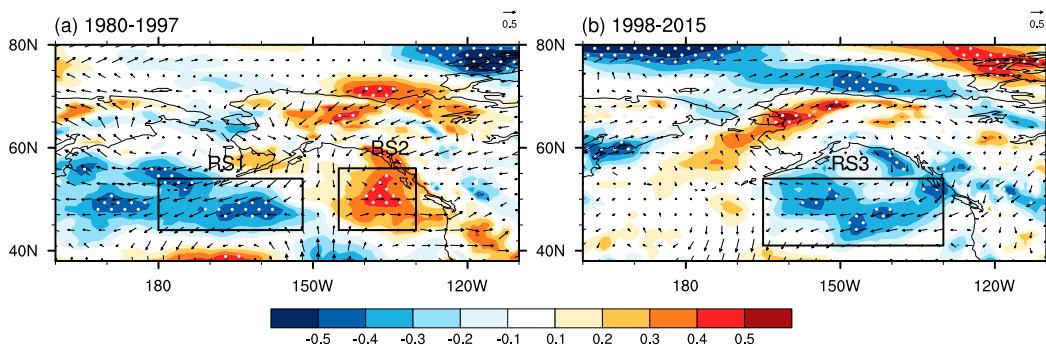


FIG. 7. The CCs between the BSISO and surface wind speed in November during (a) 1980–97 and (b) 1998–2015 after detrending. The white dots indicate CCs exceeding the 90% confidence level (t test). The black boxes (RS1, RS2, and RS3) represent the significantly correlated areas, which were used to calculate the $WSPD_{RS2-RS1}$ and $WSPD_{RS3}$ indexes. The linear trend was removed.

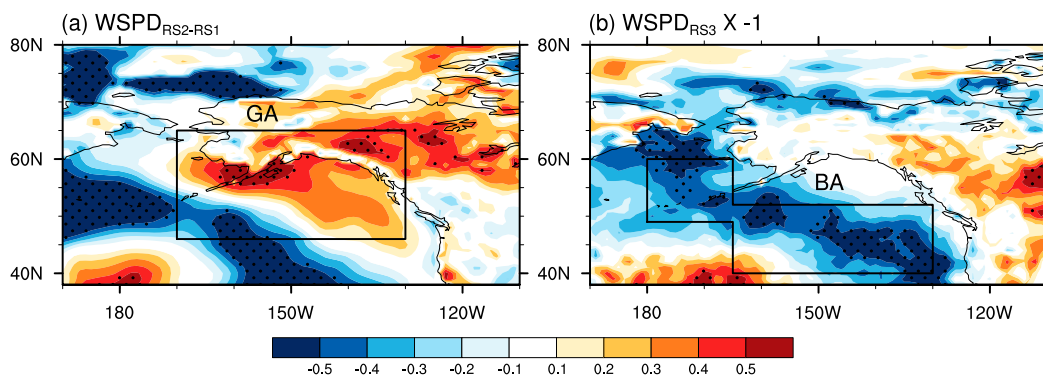


FIG. 8. The CCs between the November heat flux (latent + sensible heat flux) and (a) $WSPD_{RS2-RS1}$ from 1980–97 and (b) $WSPD_{RS3} \times -1$ from 1998–2015. The black dots indicate that the CCs exceeded the 95% confidence level (t test). The black box in (a) represents the GA area and in (b) represents the BA area. The linear trend was removed.

consequent December–January haze days. After removing the linear trend, the CCs between the SST index and HDJ_{NC} were -0.30 (SST_{GA} ; not significant) and 0.76 (SST_{BA} ; above the 99% confidence level). We speculated that the strengthened responses of haze days after the mid-1990s might be ascribed to the SST anomalies, which were evoked by the anomalous BSISO index. During P2, the positive SST anomalies heated the atmosphere and caused ascending motion over the Aleutian area (Fig. 9). Based on the anomalous ascending motion, three anomalous centers appeared in the upper troposphere, located in the northern Pacific (cyclonic circulations) and in North China and Canada (the anticyclonic circulations; Figs. 9a,b). Due to the

anticyclonic and cyclonic anomalies, the pressure gradient between North China and the Sea of Okhotsk in the Pacific enhanced, and the zonal west winds moved northward. Thus, the East Asian jet stream receded (Fig. 9a), the south section of the deep trough over East Asia weakened (Fig. 9b), and the meridionality of the atmosphere reduced, demonstrating that cold air intrusion into China receded. These anomalous atmospheric circulations favor haze pollution.

Near the surface, the strengthened and widened Aleutian low, which was ascribed to positive SST_{BA} anomalies, could evoke positive SLP anomalies in the western Pacific similar to the North Pacific Oscillation pattern (Figs. 9c,d). It is obvious that the positive SLP

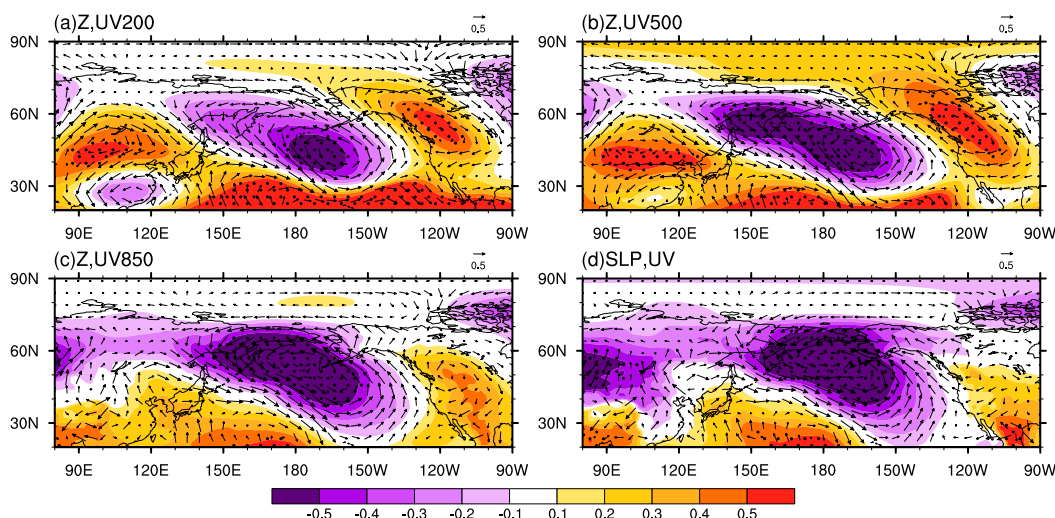


FIG. 9. The CCs between the November SST_{BA} and wind (arrow) and geopotential height (shading) at (a) 200, (b) 500, and (c) 850 hPa, and the (d) surface wind (arrow) and SLP (shading) in December–January during 1998–2015. The black dots indicate that the CCs exceeded the 95% confidence level (t test). The linear trend was removed.

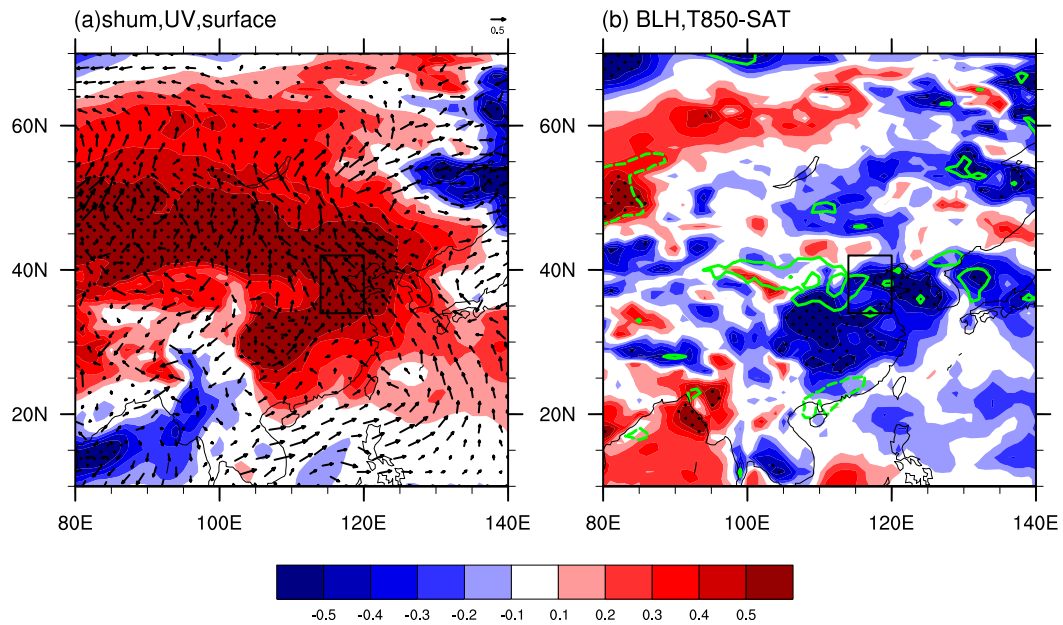


FIG. 10. The CCs between the November SST_{BA} and the (a) surface wind (arrow) and specific humidity (shading) at 1000 hPa and the (b) BLH (shading) and thermal inversion potential (contours; solid (dashed) green lines indicate that the positive (negative) correlations exceeded the 95% confidence level (*t* test) during 1998–2015. The black dots indicate that the CCs exceeded the 95% confidence level (*t* test). The linear trend was removed. The black boxes represent the NC area. The thermal inversion potential was defined as the air temperature at 850 hPa minus the surface air temperature.

anomalies caused southerly anomalies from the west Pacific to the NC area. Simultaneously, the anomalous southerlies suppressed the cold air, reduced the wind speed locally, and strengthened the transportation of humid airflow (Fig. 10a). Adequate moisture provided a feasible condition for the hygroscopic growth of fine particles, which is important for obstructing visibility. The low BLH and thermal inversion layer led to stable weather conditions by limiting the vertical dispersion (Fig. 10b). Additionally, there were obvious ascending motion anomalies over the NC area (Fig. 11b). Zhong et al. (2019) considered that the updraft could hinder the downward transport of momentum and clear air from the upper troposphere. Thus, ascending motion anomalies over the NC area were favorable for further maintaining stable weather conditions (Fig. 11b). These weather conditions, with the aforementioned atmospheric circulations, increased the occurrence of haze or deepened the degree of haze pollution.

However, during P1, the negative SST anomalies in GA cooled the atmosphere and caused a sinking motion, with weak anticyclonic responses over the Aleutian area (Fig. 12). The anomalous anticyclone responses could extend to north of Eurasia in the upper troposphere. Contrary to the P2 period, although the atmospheric circulations in the upper troposphere were not conducive to haze pollution, the weaker responses could not

contribute much to haze pollution. Near the surface, the relatively local responses during P1 were un conducive to haze pollution, such as dry and cold winds (Fig. 13a), an unstable boundary layer (Fig. 13b), and ascending motion (Fig. 14b). However, these atmospheric circulations and meteorological conditions were weak, which was the main reason for the indifferent correlations before the mid-1990s.

6. Verifications by large-ensemble numerical experiments

Numerical experiments with the CESM-LE dataset during 1980–2015 were designed to verify the aforementioned conclusions. As statistical analysis, it should be logical to design numerical experiments based on two subperiods, respectively. However, the simulated Beaufort Sea ice concentrations could not perfectly reproduce the changing features of sea ice in P1 and P2 (i.e., only the southernmost part of Beaufort Sea was dominated by seasonal ice during P1, but the replacement of perennial ice with annual ice occurred in the north of Beaufort Sea area during P2). This phenomenon somewhat reflects the limitations of climate models to simulate detailed varying features in the Arctic region (Song and Liu 2017). What we emphasized is the interannual to decadal variation and relationships by

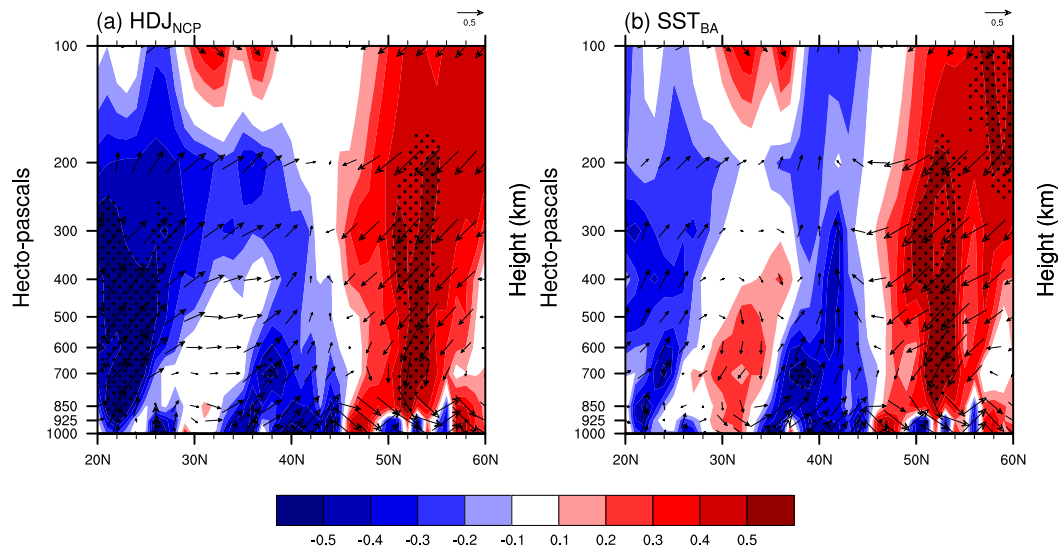


FIG. 11. The cross section (114° – 120° E mean) CCs between the (a) HDJ_{NCP} and (b) November SST_{BA} and the omega (shading) and wind (arrow) fields in December–January during 1998–2015. The black dots indicate that the CCs exceeded the 95% confidence level (t test). The linear trend was removed.

removing the linear trends. The fundamental point that caused the different physical mechanisms in two sub-periods was whether the sea ice area in the north of Beaufort Sea showed obvious variability.

As said above, if the sea ice in the north of Beaufort Sea did not melt (i.e., the multiyear sea ice was maintained), the variability of BSI_{N} was quite small (Fig. 2a). In this study, we used the melting situations of sea ice in north of Beaufort Sea to divide the samples of CESM-LE into two experiments: Experiment S (Exp-S) and

Experiment N (Exp-N). As shown in Fig. 15a (Exp-S), the mean sea ice concentration in the north of Beaufort Sea was larger than 94%, indicating a weak possibility of melting. However, those in Exp-N were in the range of 80%–94% (Fig. 15b), indicating large variability of BSI_{N} . Furthermore, the RSD of BSI_{N} in Exp-N was more than twice that in Exp-S. The scatterplot in Fig. 15c presents the sea ice area (BSI_{N} and BSI_{S} in Exp-N, BSI_{N} and BSI_{S} in Exp-S). Obviously, the BSI_{N} in Exp-N shows more dramatic dispersion (large variability) and

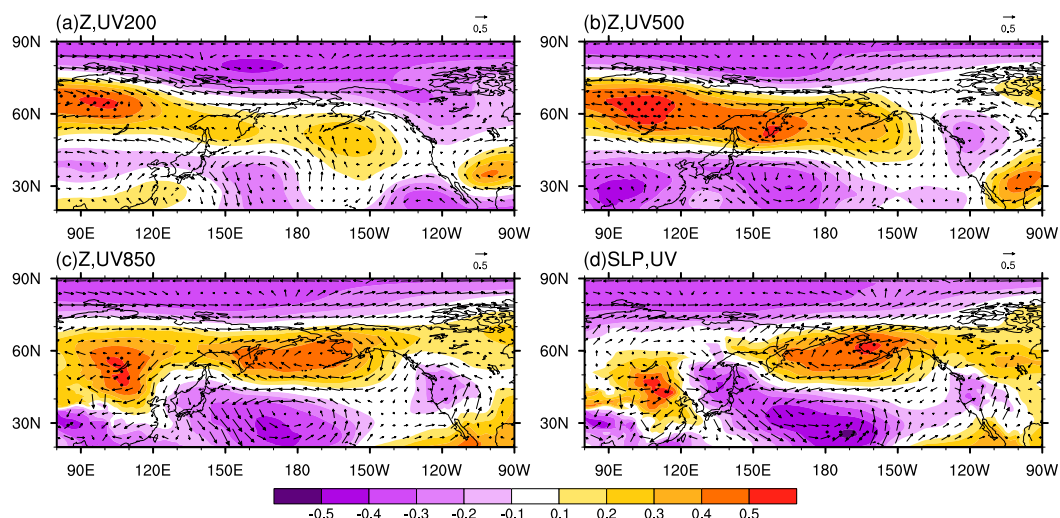


FIG. 12. The CCs between the November $\text{SST}_{\text{GA}} \times -1$ and the wind (arrow) and geopotential height (shading) at (a) 200, (b) 500, (c) and 850 hPa, and the (d) surface wind (arrow) and SLP (shading) in December–January during 1980–97. The black dots indicate that the CCs exceeded the 95% confidence level (t test). The linear trend was removed.

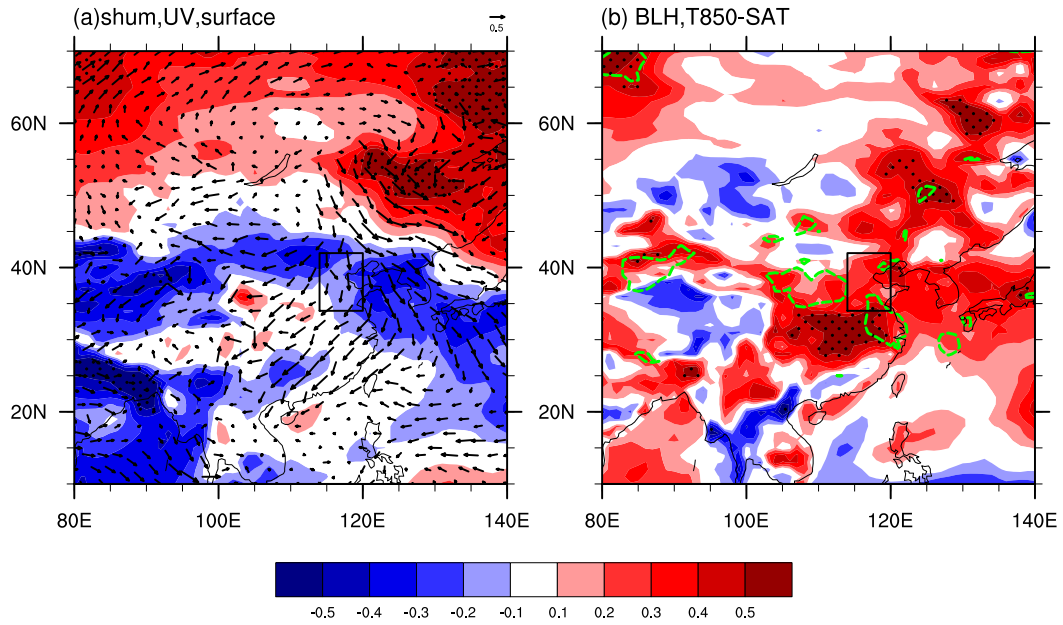


FIG. 13. The CCs between the November $SST_{GA} \times -1$ and the (a) surface wind (arrow) and specific humidity (shading) at 1000 hPa and the (b) BLH (shading) and thermal inversion potential (contour; solid (dashed) green lines indicate that the positive (negative) correlations exceeded the 95% confidence level (t test) during 1980–97. The black dots indicate that the CCs exceeded the 95% confidence level (t test). The linear trend was removed. The black boxes represent the NC area. The thermal inversion potential was defined as the air temperature at 850 hPa minus the surface air temperature.

has smaller values (melting) than those in Exp-S (Fig. 15c). Therefore, it is evident that the variability of both BSI_N and BSI_S in Exp-N was greater than those in Exp-S, which was consistent with the varying feature of sea ice after the mid-1990s. Afterward, according to

the simulated sea ice area, the samples in each experiment were divided in half, into samples with high sea ice area (HighS) and samples with low sea ice area (LowS). The composite results (HighS minus LowS) of atmospheric circulations can be considered as the relevant

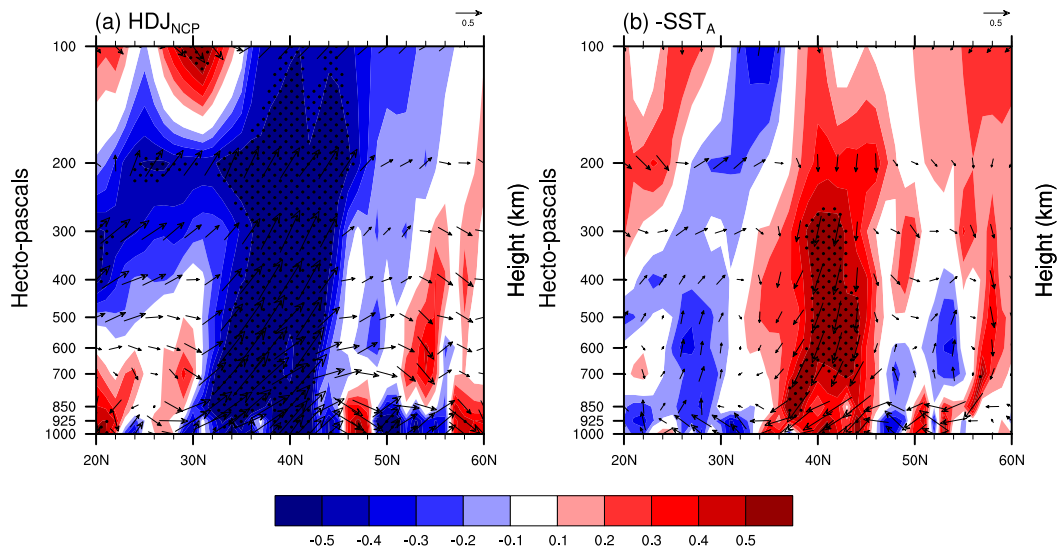


FIG. 14. The cross section (114° – 120° E mean) CCs between the (a) HDJ_{NC} and (b) November $SST_{GA} \times -1$ and the omega (shading) and wind (arrow) fields in December–January during 1980–97. The black dots indicate that the CCs exceeded the 95% confidence level (t test). The linear trend was removed.

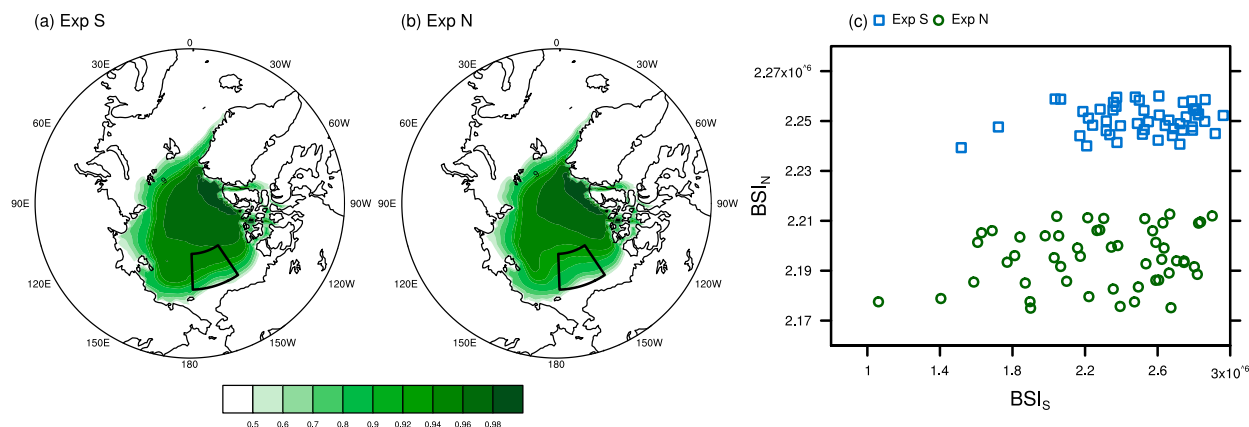


FIG. 15. Mean of September–October sea ice concentration in (a) Exp-S and (b) Exp-N. (c) Scatterplot of BSI_N and BSI_S in Exp-S (blue rectangle) and Exp-N (green circle). Results are based on 35 ensembles of CESM-LE simulations. The black box in (a) and (b) represents the location of the Beaufort Sea.

atmospheric responses associated with differences in sea ice. Furthermore, the comparisons (between the results of Exp-S and Exp-N) were used to examine the impacts of varying features of sea ice on the revealed enhancement of relationships in section 4.

Under Exp-N, relevant atmospheric responses and local weather conditions were calculated (Fig. 16). Consistent with the observations and statistical analyses, positive November SST responses were obvious in BA regions (Fig. 16a), which followed strong multiyear ice melting in entire Beaufort Sea (Fig. 15b). The early winter anticyclonic responses over NC were well simulated, both at 500 hPa or near the surface (Fig. 16b), which accorded with the observed results (Figs. 9b,c). Anticyclonic circulations in the midtroposphere caused a westerly jet moving northward and the south section of East Asian trough receded. Thus, cold activities of the atmosphere were reduced and the diffusion of pollution particles was restricted. Simultaneously, composites of local meteorological elements were also well reproduced by the numerical model in early winter (Figs. 16b,c). Anomalous southerlies, weak surface wind speed, and low BLH could limit the horizontal and vertical dispersion conditions, which were apt to the accumulation of haze particles. Moreover, adequate moisture favored fine particles growing into haze nuclei through moisture absorption (Fig. 16b), leading to reduced visibility.

The sea ice melting mainly concentrated in the south of Beaufort Sea in Exp-S (Fig. 17a) also presented results corresponding with the observations (Fig. 6a). Cumulative sea ice decreased the SST over the Gulf of Alaska in November. In the subsequent December–January, the responses of the atmospheric circulations were not significant in the midlower troposphere

(Fig. 17b). Anomalous northerlies over North China, which slightly enhance the intrusions of cold air, reappeared in the numerical experiments (Figs. 17b and 12c). Additionally, strong surface wind speed and high BLH led to unstable weather conditions (Figs. 17b,c), in accord with the above analysis (Figs. 13a,b). However, sufficient moisture was conducive to the hygroscopic growth of fine particles in NC. Thus, under the multi-factor functioning (conflicting to some extent), the effect on the haze pollution was insignificant.

When the replacement of perennial ice with annual ice occurred in the north of the Beaufort Sea (verified by Exp-N), the following November SST anomalies, as a bridge, effectively induced haze pollution over NC. When the main change of the multiyear ice occurred only on the edge of the Beaufort Sea (verified by Exp-S), there was no significant linkage of sea ice and number of haze days. The proposed physical mechanisms were successfully reproduced and the major physical processes were well captured by CESM-LE. To some extent, it shows that the proposed relationship was enhanced and demonstrates its dependence on the location of sea ice melting.

7. Conclusions and discussion

Considering the evident effect of the ASI on the midlatitude climate, we found that the correlation between September–October sea ice in the Beaufort Sea and December–January haze days in North China increased after the mid-1990s. From 1998 to 2015, the correlation coefficient between the $BSISO$ and HDJ_{NC} was 0.56 (exceeding the 99% confidence level) and was much greater than that in the first subperiod (i.e., 0.11). Furthermore, we analyzed the varying features of sea ice and found that the replacement of perennial sea ice with

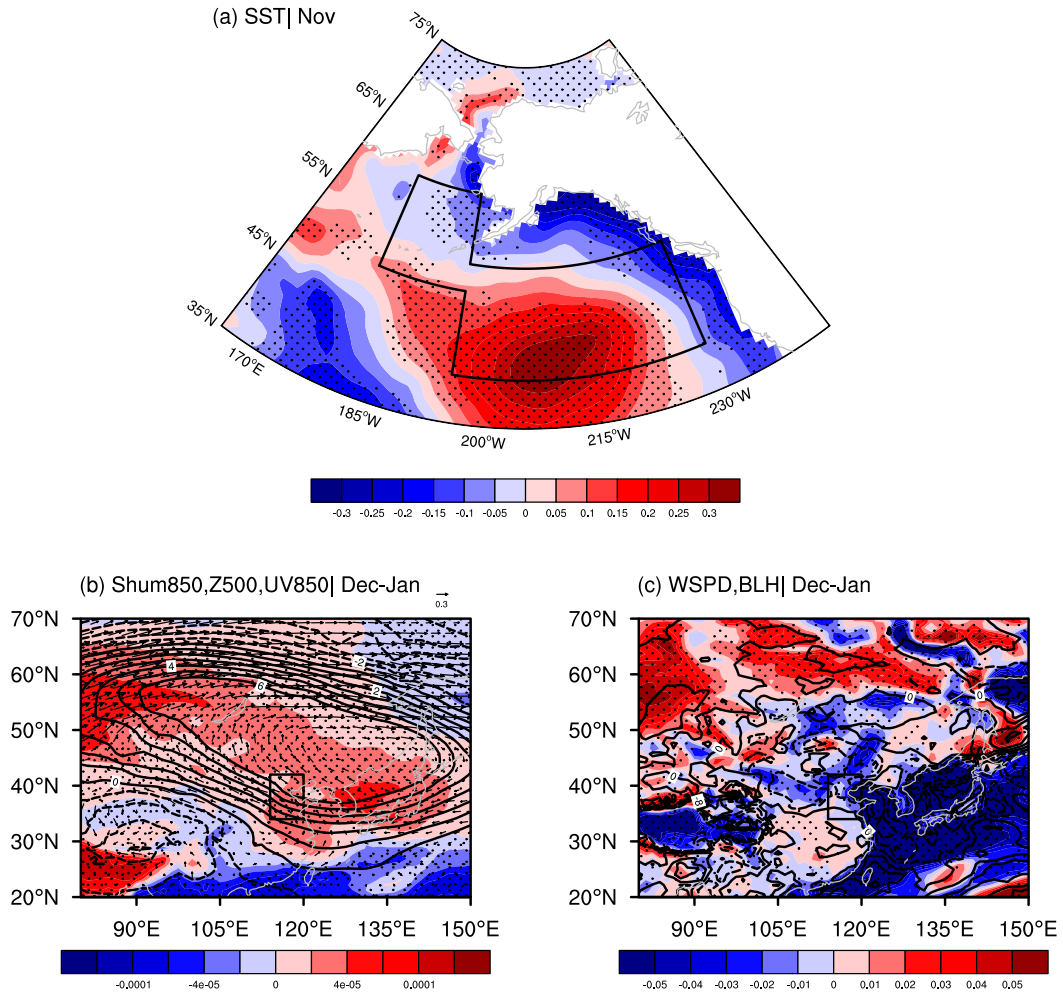


FIG. 16. Composite results in Exp-N (HighS minus LowS), including (a) sea surface temperature in November; (b) geopotential height (contour) at 500 hPa, specific humidity (shading), and wind (arrow) at 850 hPa in December–January; and (c) WSPD (shading) and BLH (contour) in December–January. The black box in (a) represents the BA area, and in (c) and (d) it represents the NC area. The black dots indicate that mathematical sign of the difference in shading are consistent with more than 55% of the members.

young ice enlarged the variability of sea ice area and strengthened the modulation effects on the atmospheric circulations. Relying on radiation cooling, the BSISO might enhance its contributions to early-winter haze in North China after the mid-1990s. In September–October, the broader sea ice cover over the Beaufort Sea would induce anomalous cyclonic circulations over the Arctic and anomalous anticyclonic circulations over the northern Pacific, causing positive SST anomalies over the Bering Sea and Gulf of Alaska in November. Due to the heating by the positive SST anomalies, the Aleutian low deepened in the following December and January, with anticyclonic anomalies occurring upstream and downstream. Under these atmospheric circulation conditions, the East Asian jet stream weakened, the south section of the deep trough over East Asia receded, and

the cold air moving southward diminished. Near the surface, the southerly anomalies, higher specific humidity, lower BLH, and a shallower thermal inversion layer led to suitable weather conditions for haze pollution. In these situations, the possibility of haze pollution was enhanced. However, from 1980 to 1997, the weak haze-associated atmospheric responses and local weather conditions, which were induced by sea ice anomalies, had difficulty to accumulating haze particles and caused a weakened contribution to haze pollution. The above-mentioned conclusions were strongly verified by the large ensemble numerical experiments.

In this study, we considered that the melting of sea ice (particularly in the north of the Beaufort Sea) played important roles in the proposed enhanced relationships. Close relationships between variations in Pacific SST

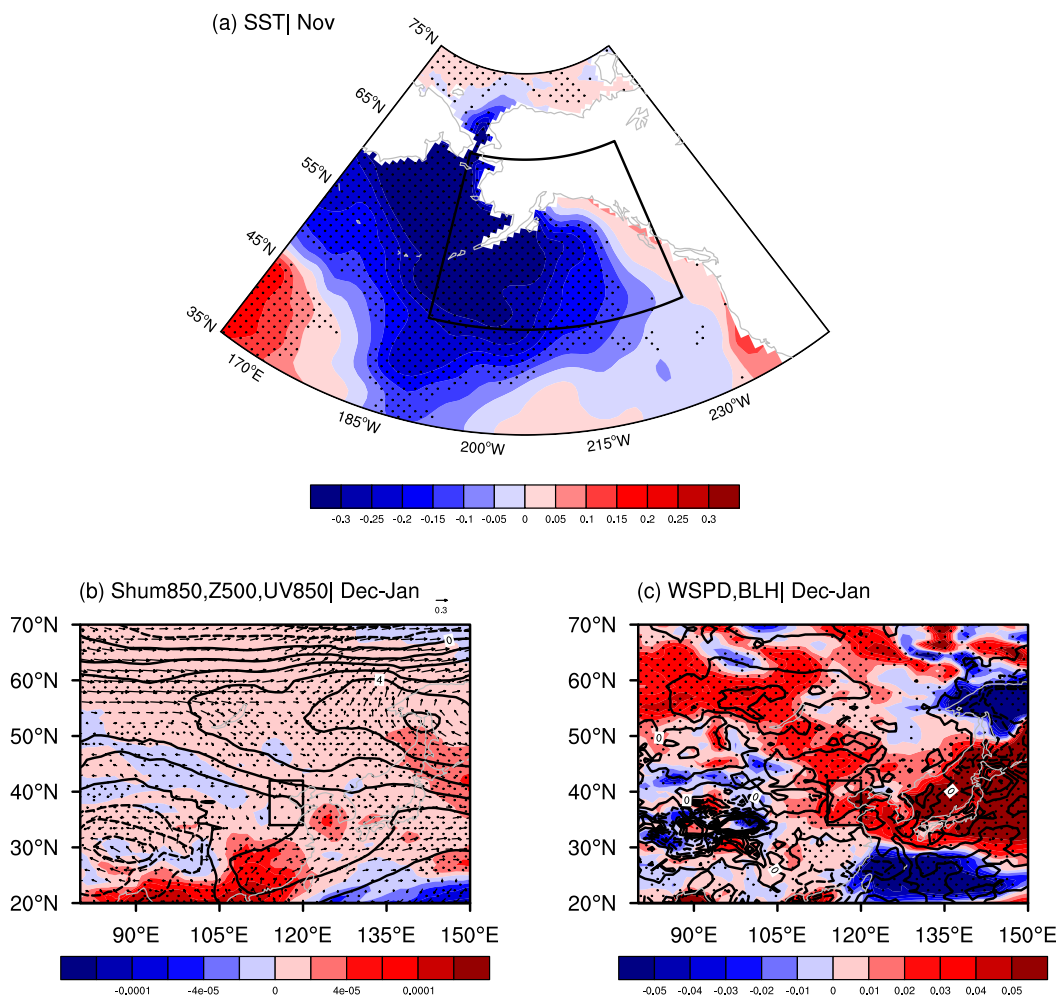


FIG. 17. Composite results in Exp-S (HighS minus LowS), including (a) SST in November; (b) geopotential height (contour) at 500 hPa, specific humidity (shading), wind (arrow) at 850 hPa in December–January; and (c) WSPD (shading) and BLH (contour) in December–January. The black box in (a) represents the BA area, and in (c) and (d) it represents the NC area. The black dots indicate that mathematical sign of the difference in shading are consistent with more than 55% of the members.

and ASI loss were posited by numerous studies. The anomalous atmospheric circulations in the high latitudes (Ding et al. 2017) and external forcings in the Pacific, such as the Pacific decadal oscillation (PDO) (Tokinaga et al. 2017), both contributed to the sea ice decline since 1979. Yu et al. (2017) pointed out that the leading mode of variability of global sea ice concentration presented remarkable declines in the Beaufort Sea and had negative correlation with the PDO. Furthermore, the contribution of sea ice loss to Arctic warming is larger during the negative PDO phase than the positive phase because both the mean circulation and sea-ice-driven anomalies during PDO negative phase are conducive to warm air advection into the Arctic (Screen and Francis 2016). The September–October PDO index was mainly positive during 1980–97 and mostly shifted to a negative

phase after the mid-1990s (Fig. 18a). According to Screen and Francis (2016), relative to the positive PDO phase, anomalous southerlies occurred and transported warm air into the north of Beaufort Sea in the negative PDO phase. These warm air advections favored the melting of sea ice (sea ice area in Fig. 18b) and thus enlarged the variability of BSISO (RSD in Fig. 18b), which resulted in more efficient modulations in the early-winter atmospheric circulations. Relying on the revealed physical mechanism in this study, the differences of HDJ_{NC} between positive and negative BSISO under the negative PDO phase are significant, but those during the positive PDO phase are insignificant (Fig. 18c). Based on these 36-yr data (mainly limited by the length of HDJ_{NC} data), the contribution of sea ice variability to haze pollution in North China is regulated

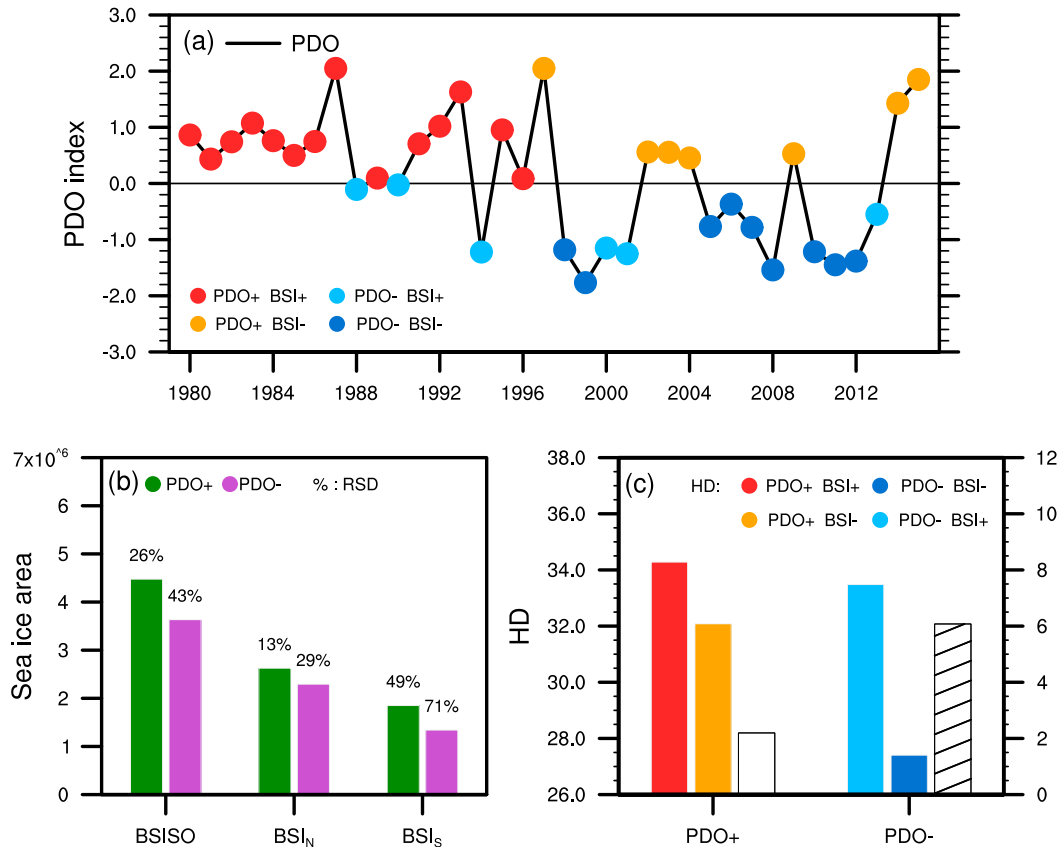


FIG. 18. (a) The variation in September–October PDO index from 1980 to 2015. The years are split into cases when the PDO index was positive (PDO+) or negative (PDO−) and the BSISO index was positive (BSI+) or negative (BSI−). (b) Composite results of BSISO, BSI_N, and BSI_S during negative PDO phase (purple bars) and positive PDO phase (green bars), respectively. The percentages were the relative standard deviation (RSD). (c) Composite results of HDJ_{NC} according to the years split in (a). The hollow bars were the differences (BSI+ minus BSI−) under the positive or negative PDO phase, where the slashes indicate the differences were significant at the 95% confidence level (*t* test).

by the phase of the PDO pattern. However, we must notice that the period of 1980–2015 only covered one to two cycles of the PDO, which would weaken the robustness of the relationships revealed in Fig. 18. In addition, Notz and Marotzke (2012) also found a physically plausible strong correlation between ASI retreat and increasing atmospheric CO₂, but very weak direct impacts from the PDO. That is, although we showed this modulating action of the PDO, there were still some uncertainties that needed longer observations and further numerical experiments, similar to Screen and Francis (2016).

Yin and Wang (2016a, 2017b) built seasonal prediction models to forecast the haze conditions in the following winter, and September–October sea ice was identified as an efficient factor. Thus, it is meaningful to assess the influences of changed relationships on the seasonal predictions. Although the enhanced contributions

of Beaufort Sea ice to early-winter haze days in North China were clearly revealed in this study, some questions were still unexplored. In this study, we choose the sea ice area to reflect the effects of sea ice on climate. Thickness and other peculiarities of sea ice, related to the melting of perennial sea ice, were not included and still required further exploration. It is also worth noting that a large number of global model simulations indicate that the sea ice-free season may prolong under global warming (Markus et al. 2009; Wang and Overland 2015); thus, the physical mechanisms, when the sea ice disappears, still need further verification. Moreover, we mainly focused on the interannual effects of sea ice concentrations in the Beaufort Sea on haze days in North China. During the analysis, the linear trend was removed to represent the characteristics of interannual variability, which is consistent with Wang et al. (2015). Ding et al. (2017) illustrated that the September sea ice

concentration over the Beaufort Sea, which was sensitive to the Arctic amplification phenomenon, remarkably decreased since 1979. Thus, in addition to the interannual connections revealed here, the trend between sea ice and haze days requires further research.

Acknowledgments. This research was supported by the National Natural Science Foundation of China (41705058 and 91744311), the National Key Research and Development Plan (2016YFA0600703), the CAS–PKU Partnership Program, and the funding of the Jiangsu Innovation and Entrepreneurship team. Author contributions: ZY designed the research. YL performed the research. ZY and YL analyzed the data. ZY and YL prepared the paper.

REFERENCES

- Alekseev, G., N. Glok, and A. Smirnov, 2016: On assessment of the relationship between changes of sea ice extent and climate in the Arctic. *Int. J. Climatol.*, **36**, 3407–3412, <https://doi.org/10.1002/joc.4550>.
- Bader, J., M. D. S. Mesquita, K. I. Hodges, N. Keenlyside, S. Østerhus, and M. Miles, 2011: A review on Northern Hemisphere sea-ice, storminess and the North Atlantic Oscillation: Observations and projected changes. *Atmos. Res.*, **101**, 809–834, <https://doi.org/10.1016/j.atmosres.2011.04.007>.
- Blackport, R., Screen, J. A. 2020: Insignificant effect of Arctic amplification on the amplitude of midlatitude atmospheric waves. *Sci. Adv.*, **6**, eaay2880, <https://doi.org/10.1126/sciadv.aay2880>.
- Cavalieri, D. J., and C. L. Parkinson, 2012: Arctic sea ice variability and trends, 1979–2010. *Cryosphere*, **6**, 881–889, <https://doi.org/10.5194/tc-6-881-2012>.
- Dang, R., and H. Liao, 2019: Severe winter haze days in the Beijing–Tianjin–Hebei region from 1985 to 2017 and the roles of anthropogenic emissions and meteorology. *Atmos. Chem. Phys.*, **19**, 10 801–10 816, <https://doi.org/10.5194/acp-19-10801-2019>.
- Dee, D. P., and Coauthors, 2011: The ERA-Interim reanalysis: Configuration and performance of the data assimilation system. *Quart. J. Roy. Meteor. Soc.*, **137**, 553–597, <https://doi.org/10.1002/qj.828>.
- Deser, C., R. A. Tomas, and S. Peng, 2007: The transient atmospheric circulation response to North Atlantic SST and sea ice anomalies. *J. Climate*, **20**, 4751–4767, <https://doi.org/10.1175/JCLI4278.1>.
- Ding, Q. A., and Coauthors, 2017: Influence of high-latitude atmospheric circulation changes on summertime Arctic sea ice. *Nat. Climate Change*, **7**, 289–295, <https://doi.org/10.1038/nclimate3241>.
- Fan, K., Z. M. Xie, H. J. Wang, Z. Q. Xu, and J. P. Liu, 2017: Frequency of spring dust weather in North China linked to sea ice variability in the Barents Sea. *Climate Dyn.*, **51**, 4439–4450, <https://doi.org/10.1007/s00382-016-3515-7>.
- Francis, J. A., and S. J. Vavrus, 2012: Evidence linking Arctic amplification to extreme weather in mid-latitudes. *Geophys. Res. Lett.*, **39**, L06801, <https://doi.org/10.1029/2012GL051000>.
- Gao, Y., and Coauthors, 2015: Arctic sea ice and Eurasian climate: A review. *Adv. Atmos. Sci.*, **32**, 92–114, <https://doi.org/10.1007/s00376-014-0009-6>.
- Guo, D., Y. Gao, I. Bethke, D. Gong, O. M. Johannessen, and H. Wang, 2014: Mechanism on how the spring Arctic sea ice impacts the East Asian summer monsoon. *Theor. Appl. Climatol.*, **115**, 107–119, <https://doi.org/10.1007/s00704-013-0872-6>.
- Holland, M. M., C. M. Bitz, and B. Tremblay, 2006: Future abrupt reductions in the summer Arctic sea ice. *Geophys. Res. Lett.*, **33**, L23503, <https://doi.org/10.1029/2006GL028024>.
- Hopsch, S., J. Cohen, and K. Dethloff, 2012: Analysis of a link between fall Arctic sea ice concentration and atmospheric patterns in the following winter. *Tellus*, **64A**, 18624, <https://doi.org/10.3402/tellusa.v64i0.18624>.
- Kay, J. E., and Coauthors, 2015: The Community Earth System Model (CESM) large ensemble project: A community resource for studying climate change in the presence of internal climate variability. *Bull. Amer. Meteor. Soc.*, **96**, 1333–1349, <https://doi.org/10.1175/BAMS-D-13-00255.1>.
- Kwok, R., 2018: Arctic sea ice thickness, volume, and multiyear ice coverage: Losses and coupled variability (1958–2018). *Environ. Res. Lett.*, **13**, 105005, <https://doi.org/10.1088/1748-9326/aae3ec>.
- , and D. A. Rothrock, 2009: Decline in Arctic sea ice thickness from submarine and ICESat records: 1958–2008. *Environ. Res. Lett.*, **36**, L15501, <https://doi.org/10.1029/2009GL039035>.
- Lee, S., T. Gong, S. B. Feldstein, J. A. Screen, and I. Simmonds, 2017: Revisiting the cause of the 1989–2009 Arctic surface warming using the surface energy budget: Downward infrared radiation dominates the surface fluxes. *Geophys. Res. Lett.*, **44**, 10 654–10 661, <https://doi.org/10.1002/2017GL075375>.
- Li, F., and H. J. Wang, 2013: Relationship between Bering Sea ice cover and East Asian winter monsoon year-to-year variations. *Adv. Atmos. Sci.*, **30**, 48–56, <https://doi.org/10.1007/s00376-012-2071-2>.
- , and —, 2014: Autumn Eurasian snow depth, autumn Arctic sea ice cover and East Asian winter monsoon. *Int. J. Climatol.*, **34**, 3616–3625, <https://doi.org/10.1002/joc.3936>.
- , —, and Y. Q. Gao, 2015: Change in sea ice cover is responsible for non-uniform variation in winter temperature over East Asia. *Atmos. Oceanic Sci. Lett.*, **8**, 376–382, <https://doi.org/10.3878/AOSL20150039>.
- Li, X. B., H. B. Liu, Z. Y. Zhang, and J. J. Liu, 2019: Numerical simulation of an extreme haze pollution event over the North China Plain based on initial and boundary condition ensembles. *Atmos. Oceanic Sci. Lett.*, **12**, 434–443, <https://doi.org/10.1080/16742834.2019.1671136>.
- Luo, B. H., D. H. Luo, L. X. Wu, L. H. Zhong, and I. Simmonds, 2017: Atmospheric circulation patterns which promote winter Arctic sea ice decline. *Environ. Res. Lett.*, **12**, 054017, <https://doi.org/10.1088/1748-9326/aa69d0>.
- Luo, D. H., Y. Q. Xiao, Y. Diao, A. G. Dai, C. L. E. Franzke, and I. Simmonds, 2016: Impact of Ural blocking on winter warm Arctic–cold Eurasian anomalies. Part II: The link to the North Atlantic Oscillation. *J. Climate*, **29**, 3949–3971, <https://doi.org/10.1175/JCLI-D-15-0612.1>.
- , X. D. Chen, A. G. Dai, and I. Simmonds, 2018: Changes in atmospheric blocking circulations linked with winter Arctic warming: A new perspective. *J. Climate*, **31**, 7661–7678, <https://doi.org/10.1175/JCLI-D-18-0040.1>.
- , —, J. Overland, I. Simmonds, Y. T. Wu, and P. F. Zhang, 2019: Weakened potential vorticity barrier linked to recent winter Arctic sea ice loss and midlatitude cold extremes. *J. Climate*, **32**, 4235–4261, <https://doi.org/10.1175/JCLI-D-18-0449.1>.

- Markus, T., J. C. Stroeve, and J. Miller, 2009: Recent changes in Arctic sea ice melt onset, freezeup, and melt season length. *J. Geophys. Res.*, **114**, C12024, <https://doi.org/10.1029/2009JC005436>.
- Maslanik, J. A., C. Fowler, J. Stroeve, S. Drobot, J. Zwally, D. Yi, and W. Emery, 2007: A younger, thinner Arctic ice cover: Increased potential for rapid, extensive sea-ice loss. *Geophys. Res. Lett.*, **34**, L24501, <https://doi.org/10.1029/2007GL032043>.
- , J. Stroeve, C. Fowler, and W. Emery, 2011: Distribution and trends in Arctic sea ice age through spring 2011. *Geophys. Res. Lett.*, **38**, L13502, <https://doi.org/10.1029/2011GL047735>.
- Mizobata, K., K. Shimada, S.-I. Saitoh, and J. Wang, 2010: Erratum to: Estimation of heat flux through the eastern Bering Strait. *J. Oceanogr.*, **66**, 885, <https://doi.org/10.1007/s10872-010-0072-2>.
- Mudryk, L. R., and Coauthors, 2018: Canadian snow and sea ice: Historical trends and projections. *Cryosphere*, **12**, 1157–1176, <https://doi.org/10.5194/tc-12-1157-2018>.
- Na, L., J. P. Liu, Z. H. Zhang, H. X. Chen, and M. R. Song, 2012: Is extreme Arctic sea ice anomaly in 2007 a key contributor to severe January 2008 snowstorm in China? *Int. J. Climatol.*, **32**, 2081–2087, <https://doi.org/10.1002/joc.2400>.
- Notz, D., and J. Marotzke, 2012: Observations reveal external driver for Arctic sea-ice retreat. *Geophys. Res. Lett.*, **39**, L08502, <https://doi.org/10.1029/2012GL051094>.
- Overland, J. E., and M. Y. Wang, 2010: Large-scale atmospheric circulation changes associated with the recent loss of Arctic sea ice. *Tellus*, **62A** (1), 1–9, <https://doi.org/10.1111/j.1600-0870.2009.00421.x>.
- , and —, 2013: When will the summer Arctic be nearly sea ice free? *Geophys. Res. Lett.*, **40**, 2097–2101, <https://doi.org/10.1002/grl.50316>.
- Peng, H. T., C. Q. Ke, X. Y. Shen, M. M. Li, and Z. D. Shao, 2019: Summer albedo variations in the Arctic sea ice region from 1982 to 2015. *Int. J. Climatol.*, <https://doi.org/10.1002/joc.6379>.
- Polyakov, I. V., J. E. Walsh, and R. Kwok, 2012: Recent changes of Arctic multiyear sea ice coverage and the likely causes. *Bull. Amer. Meteor. Soc.*, **93**, 145–151, <https://doi.org/10.1175/BAMS-D-11-00070.1>.
- , and Coauthors, 2017: Greater role for Atlantic inflows on sea-ice loss in the Eurasian basin of the Arctic Ocean. *Science*, **356**, 285–291, <https://doi.org/10.1126/science.aai8204>.
- Rayner, N. A., D. E. Parker, E. B. Horton, C. K. Folland, L. V. Alexander, D. P. Rowell, E. C. Kent, and A. Kaplan, 2003: Global analyses of sea surface temperature, sea ice, and night marine air temperature since the late nineteenth century. *J. Geophys. Res.*, **108**, 4407, <https://doi.org/10.1029/2002JD002670>.
- Rigor, I. G., J. M. Wallace, and R. L. Colony, 2002: Response of sea ice to the Arctic Oscillation. *J. Climate*, **15**, 2648–2663, [https://doi.org/10.1175/1520-0442\(2002\)015<2648:ROSITT>2.0.CO;2](https://doi.org/10.1175/1520-0442(2002)015<2648:ROSITT>2.0.CO;2).
- Screen, J. A., and I. Simmonds, 2010a: The central role of diminishing sea ice in recent Arctic temperature amplification. *Nature*, **464**, 1334–1337, <https://doi.org/10.1038/nature09051>.
- , and —, 2010b: Increasing fall–winter energy loss from the Arctic Ocean and its role in Arctic temperature amplification. *Geophys. Res. Lett.*, **37**, L16707, <https://doi.org/10.1029/2010GL044136>.
- , and J. Francis, 2016: Contribution of sea-ice loss to Arctic amplification is regulated by Pacific Ocean decadal variability. *Nat. Climate Change*, **6**, 856–860, <https://doi.org/10.1038/nclimate3011>.
- , I. Simmonds, and K. Keay, 2011: Dramatic interannual changes of perennial Arctic sea ice linked to abnormal summer storm activity. *J. Geophys. Res.*, **116**, D15105, <https://doi.org/10.1029/2011JD015847>.
- , T. J. Bracegirdle, and I. Simmonds, 2018: Polar climate change as manifest in atmospheric circulation. *Curr. Climate Change Rep.*, **4**, 383–395, <https://doi.org/10.1007/s40641-018-0111-4>.
- Shimada, K., T. Kamoshida, M. Itoh, S. Nishino, E. Carmack, F. McLaughlin, S. Zimmermann, and A. Proshutinsky, 2006: Pacific Ocean inflow: Influence on catastrophic reduction of sea ice cover in the Arctic Ocean. *Geophys. Res. Lett.*, **33**, L08605, <https://doi.org/10.1029/2005GL025624>.
- Simmonds, I., 2015: Comparing and contrasting the behaviour of Arctic and Antarctic sea ice over the 35-year period 1979–2013. *Ann. Glaciol.*, **56**, 18–28, <https://doi.org/10.3189/2015AoG69A909>.
- , and K. Keay, 2009: Extraordinary September Arctic sea ice reductions and their relationships with storm behavior over 1979–2008. *Geophys. Res. Lett.*, **36**, L19715, <https://doi.org/10.1029/2009GL039810>.
- , C. Burke, and K. Keay, 2008: Arctic climate change as manifest in cyclone behavior. *J. Climate*, **21**, 5777–5796, <https://doi.org/10.1175/2008JCLI2366.1>.
- Song, M. R., and J. P. Liu, 2017: The role of diminishing Arctic sea ice in increased winter snowfall over northern high-latitude continents in a warming environment. *Acta Oceanol. Sin.*, **36**, 34–41, <https://doi.org/10.1007/s13131-017-1021-3>.
- Steele, M., W. Ermold, and J. Zhang, 2008: Arctic Ocean surface warming trends over the past 100 years. *Geophys. Res. Lett.*, **35**, L02614, <https://doi.org/10.1029/2007GL031651>.
- Subrahmanyam, D. B., S. I. Rani, R. Ramachandran, P. K. Kunhikrishnan, and B. P. Kumar, 2009: Impact of wind speed and atmospheric stability on air–sea interface fluxes over the East Asian marginal seas. *Atmos. Res.*, **94**, 81–90, <https://doi.org/10.1016/j.atmosres.2008.09.011>.
- Tang, Q. H., X. J. Zhang, X. H. Yang, and J. A. Francis, 2013: Cold winter extremes in northern continents linked to Arctic sea ice loss. *Environ. Res. Lett.*, **8**, 014036, <https://doi.org/10.1088/1748-9326/8/1/014036>.
- Tokinaga, H., S. P. Xie, and H. Mukougawa, 2017: Early 20th-century Arctic warming intensified by Pacific and Atlantic multidecadal variability. *Proc. Natl. Acad. Sci. USA*, **114**, 6227–6232, <https://doi.org/10.1073/pnas.1615880114>.
- Tschudi, M., W. N. Meier, J. S. Stewart, C. Fowler, and J. Maslanik, 2019: EASE-Grid Sea Ice Age, version 4. NASA National Snow and Ice Data Center Distributed Active Archive Center, accessed 16 July 2019, <https://doi.org/10.5067/UTAV7490FEPB>.
- Vihma, T., 2014: Effects of Arctic sea ice decline on weather and climate: A review. *Surv. Geophys.*, **35**, 1175–1214, <https://doi.org/10.1007/s10712-014-9284-0>.
- Wang, H. J., and H. P. Chen, 2016: Understanding the recent trend of haze pollution in eastern China: Role of climate change. *Atmos. Chem. Phys.*, **16**, 4205–4211, <https://doi.org/10.5194/acp-16-4205-2016>.
- , —, and J. P. Liu, 2015: Arctic sea ice decline intensified haze pollution in eastern China. *Atmos. Oceanic Sci. Lett.*, **8** (1), 1–9, <https://doi.org/10.3878/AOSL20140081>.
- Wang, M., and J. E. Overland, 2015: Projected future duration of the sea-ice-free season in the Alaskan Arctic. *Prog. Oceanogr.*, **136**, 50–59, <https://doi.org/10.1016/j.pocean.2015.01.001>.
- , Q. Yang, J. E. Overland, and P. Stabeno, 2017: Sea-ice cover timing in the Pacific Arctic: The present and projections to mid-century by selected CMIP5 models. *Deep-Sea Res. II*, **152**, 22–34, <https://doi.org/10.1016/J.DSR2.2017.11.017>.

- Wang, S. Y., and J. P. Liu, 2016: Delving into the relationship between autumn Arctic sea ice and central–eastern Eurasian winter climate. *Atmos. Oceanic Sci. Lett.*, **9**, 366–374, <https://doi.org/10.1080/16742834.2016.1207482>.
- Wu, B. Y., and R. H. Zhang, 2009: On the association between spring Arctic sea ice concentration and Chinese summer rainfall: A further study. *Adv. Atmos. Sci.*, **26**, 666–678, <https://doi.org/10.1007/s00376-009-9009-3>.
- Wu, R. G., and J. L. Kinter, 2011: Shortwave radiation–SST relationship over the mid-latitude North Pacific during boreal summer in climate models. *Climate Dyn.*, **36**, 2251–2264, <https://doi.org/10.1007/s00382-010-0775-5>.
- Yang, Y., H. Liao, and S. Lou, 2016: Increase in winter haze over eastern China in recent decades: Roles of variations in meteorological parameters and anthropogenic emissions. *J. Geophys. Res. Atmos.*, **121**, 13 050–13 065, <https://doi.org/10.1002/2016JD025136>.
- Yin, Z. C., and H. J. Wang, 2016a: Seasonal prediction of winter haze days in the north central North China Plain. *Atmos. Chem. Phys.*, **16**, 14 843–14 852, <https://doi.org/10.5194/acp-16-14843-2016>.
- , and —, 2016b: The relationship between the subtropical western Pacific SST and haze over north-central North China Plain. *Int. J. Climatol.*, **36**, 3479–3491, <https://doi.org/10.1002/joc.4570>.
- , and —, 2017a: Role of atmospheric circulations on haze pollution in December 2016. *Atmos. Chem. Phys.*, **17**, 11 673–11 681, <https://doi.org/10.5194/acp-17-11673-2017>.
- , and —, 2017b: Statistical prediction of winter haze days in the North China Plain using the generalized additive model. *J. Appl. Meteor. Climatol.*, **56**, 2411–2419, <https://doi.org/10.1175/JAMC-D-17-0013.1>.
- , —, and D. M. Yuan, 2015: Interdecadal increase of haze in winter over North China and the Huang-huai area and the weakening of the East Asia winter monsoon (in Chinese). *Chin. Sci. Bull.*, **60**, 1395–1400, <https://doi.org/10.1360/N972014-01348>.
- , Y. Y. Li, and H. J. Wang, 2019: Response of early winter haze in the North China Plain to autumn Beaufort Sea ice. *Atmos. Chem. Phys.*, **19**, 1439–1453, <https://doi.org/10.5194/acp-19-1439-2019>.
- Yu, L., S. Zhong, J. A. Winkler, M. Zhou, D. H. Lenschow, B. Li, X. Wang, and Q. Yang, 2017: Possible connections of the opposite trends in Arctic and Antarctic sea-ice cover. *Sci. Rep.*, **7**, 45804, <https://doi.org/10.1038/srep45804>.
- Zhong, W. G., Z. C. Yin, and H. J. Wang, 2019: The relationship between the anticyclonic anomalies in northeast Asia and severe haze in the Beijing–Tianjin–Hebei region. *Atmos. Chem. Phys.*, **19**, 5941–5957, <https://doi.org/10.5194/acp-19-5941-2019>.
- Zhou, W., 2017: Impact of Arctic amplification on East Asian winter climate. *Atmos. Oceanic Sci. Lett.*, **10**, 385–388, <https://doi.org/10.1080/16742834.2017.1350093>.